Check for updates

AGU ADVANCING EARTH AND SPACE SCIENCE

Tectonics

RESEARCH ARTICLE
10.1029/2020TC006644

Key Points:

- Lithospheric deformation in the Strait of Hormuz syntaxis inferred from seismic anisotropy
- Transition from ophiolite obduction to early continental collision resulted in ~90° rotation of the crustal-anisotropy fast directions
- Geophysical evidence from the mantle lithosphere of NE polarity of the Late Cretaceous Oman subduction zone system

Supporting Information:

Supporting Information may be found in the online version of this article.

Correspondence to:

S. Pilia,
sp895@cam.ac.uk

Citation:

Pilia, S., Kaviani, A., Searle, M. P., Arroucau, P., Ali, M. Y., & Watts, A. B. (2021). Crustal and mantle deformation inherited from obduction of the Semail ophiolite (Oman) and continental collision (Zagros). *Tectonics*, *40*, e2020TC006644. https://doi.org/10.1029/2020TC006644

Received 26 NOV 2020
Accepted 21 MAY 2021

© Wiley Periodicals LLC. The Authors. This is an open access article under the terms of the Creative Commons Attribution License, which permits use, distribution and reproduction in any medium, provided the original work is properly cited.

Crustal and Mantle Deformation Inherited From Obduction of the Semail Ophiolite (Oman) and Continental Collision (Zagros)

S. Pilia[1], A. Kaviani[2], M. P. Searle[3], P. Arroucau[4], M. Y. Ali[5], and A. B. Watts[3]

[1]Department of Earth Sciences-Bullard Labs, University of Cambridge, Cambridge, UK, [2]Institute of Geosciences, Goethe University Frankfurt, Frankfurt, Germany, [3]Department of Earth Sciences, University of Oxford, Oxford, UK, [4]Electricité de France, Direction Industrielle, TEGG, Aix-en-Provence, France, [5]Department of Earth Sciences, Khalifa University of Science and Technology, Abu Dhabi, UAE

Abstract A common deviation from typical subduction models occurs when thrust sheets of oceanic crust and upper-mantle rocks are emplaced over more buoyant continental lithosphere. The archetypal example of ophiolite obduction is the Semail ophiolite in the United Arab Emirates (UAE)-Oman orogenic belt, formed and obducted onto the Arabian continental margin during the Late Cretaceous. The Strait of Hormuz syntaxis, the northern extent of the UAE-Oman mountains, marks the transition from ocean-continent convergence in the Gulf of Oman to continental collision along the Zagros Mountains. Based on new seismic data from a focused recording network, we infer continental crustal and mantle deformation in the northeastern corner of the Arabian plate (including the southern Zagros and the UAE-Oman mountains), using observations from anisotropic tomography and shear-wave splitting (SWS) measurements. We recover a change of ~90° (from approximately WNW to nearly NS) in the axis of fast-anisotropic orientations in the crust from the Zagros to the UAE-Oman mountain belt, consistent with the dominant strike of the orogenic belts. We also find evidence in our SWS parameters for localized fossil deformation in the lithospheric mantle underlying the UAE-Oman mountain range, possibly related to stress-induced tectonism triggered by north-east oriented underthrusting of the proto-Arabian continental margin beneath the overriding Semail ophiolite. Shear-wave-splitting anisotropy orientations along two transects across the northern Musandam peninsula, averaging 15° anticlockwise from the north, provide the first geophysical verification of previous geological evidence that suggests a NE polarity of the Late Cretaceous Oman subduction zone system.

1. Introduction

The northeastern corner of the Arabian plate, from the Oman-UAE mountains around the Strait of Hormuz syntaxis to the Zagros Mountains in Iran, provides an excellent framework for understanding plate kinematics and geodynamics during the transition from ophiolite obduction to early continent-continent collision (Carminati et al., 2020; Glennie et al., 1973; Searle, 2007, 2019). Indeed, the converging motion between the Arabian and Eurasian plates drives a major structural segment of the Alpine-Himalayan chain and seismic activity in the Zagros fold-and-thrust-belts (ZFTB – Figure 1). The Strait of Hormuz syntaxis in the Musandam Peninsula is the transition from the ocean-continent boundary in the Gulf of Oman to the continent-continent collision along the Zagros Mountains in Iran (Searle, 1988; Searle et al., 2014).

Tectonic processes that affected the northeastern Arabian margin include (i) continental accretion during the Precambrian-Cambrian, multiple rifting events with accompanying basin subsidence and shelf carbonate deposition from Early Permian to Early Jurassic, post-rift stable sedimentary conditions (see Stern & Johnson, 2010, for a review of the Arabian plate), (ii) emplacement of the Semail ophiolite in Late Cretaceous and uplift of the UAE-Oman mountains (see Searle, 2019, for a review), and (iii) continental collision between the former Arabian passive margin and central Iran from Early Eocene (see Agard et al., 2011, for a review). The Semail ophiolite in the UAE-Oman belt is arguably the world's best example of an obducted ophiolite complex. The ophiolite formed at a fast-spreading ridge above a NE-dipping subduction zone at ca. 96.5–95 Ma (Rioux et al., 2016; Tilton et al., 1981), followed immediately by its emplacement from NE to SW onto the previously passive continental margin of Arabia. A series of allochthonous thrust sheets (Haybi and Hawasina complex thrust sheets) were emplaced structurally beneath the ophiolite to the southwest

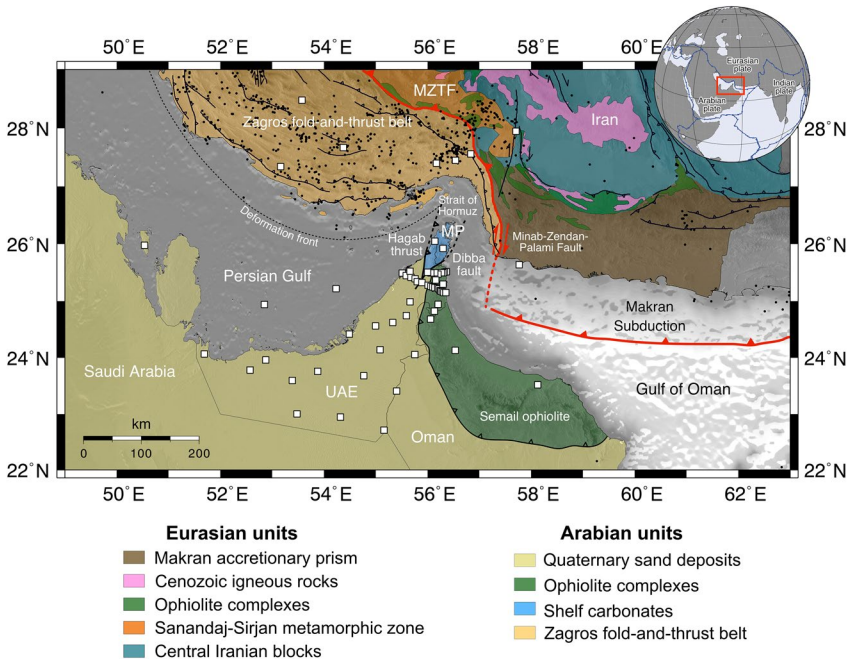

Figure 1. Simplified tectonic map of the study area as modified from the National Geoscience Database of Iran. Black lines are major faults; in the Zagros, these are generally inferred from abrupt changes in the stratigraphic level within the Mesozoic sedimentary section. Red line is the suture boundary (MZTF: Main Zagros Thrust Fault) between the Arabian platform and central Iran. Black dots are earthquakes from the ISC catalog. White squares are seismic stations. Background map represents shaded relief. The inset in the upper right corner shows the location of the study area. MP, Musandam Peninsula.

onto the Permian-Mesozoic shelf carbonate sequence of the Arabian passive margin (Glennie et al., 1973; Searle, 2007). The resulting orogeny is the last major tectonic event that shaped the crust of the UAE and Oman, although mid-Cenozoic and late-Cenozoic events uplifted the mountain chain by up to ca 2 km (Glennie et al., 1974; Searle, 2019). Based on paleomagnetic evidence, Morris et al. (2016) proposed that the entire ophiolite was rotated clockwise by ~90° during obduction, although there is little evidence for this from the surface geology of the ophiolite and all allochthonous units beneath, or any kinematic restoration (Searle, 2019). The earliest effects of the subsequent collision between Arabia and central Iran along the Zagros suture zone (~23–16 Ma) are seen in the northernmost Musandam Peninsula where Oligocene-early Miocene thrusting along the Hagab thrust records initial crustal shortening and thickening (Ali et al., 2017; Searle, 1988; Searle et al., 2014). The Musandam Peninsula and its extension offshore show a tight 90° bend in the strike of the orogenic belts from the southern Zagros Mountains to the UAE-Oman belt. This region has been interpreted as representing an early stage of a major orogenic-syntaxis development, analogous to the Nanga Parbat and Namche Barwa syntaxes in the Himalaya (Searle, 2015).

Previous seismic tomographic models of the study region have been coarse (e.g., Priestley et al., 2012) and, even if they have been able to illuminate relatively small structure, typically assume isotropic variations of the seismic wavefield (e.g., Pilia et al., 2020a; Pilia et al., 2020b). This means that observational constraints on crustal and mantle deformation in the form of anisotropy are not retrieved. The lack of anisotropy information has prevented previous studies from making inferences on how the lithosphere has been deformed due to complex processes such as obduction of the Semail ophiolite (and preceding subduction) and indentation of the Musandam Peninsula. A number of mechanisms are responsible for the directional dependence of seismic wave-speed but regular patterns of tectonic fabric, stress-aligned microcracks, and preferred mineral alignment are generally invoked in anisotropic lithospheric studies (Babuska & Cara, 1991; Crampin, 1994). For instance, areas subject to major deformation events (e.g., orogenic belts, extensional domains) tend to inherit an anisotropic signature that is congruent with the strike of regional tectonic structures.

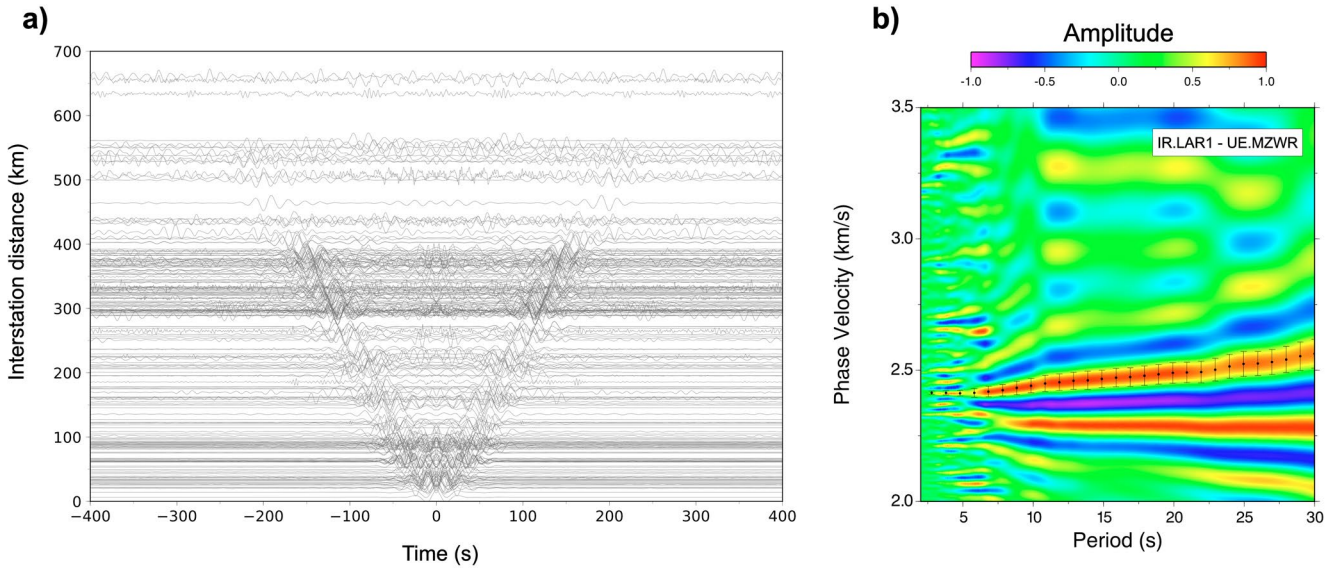

Figure 2. (a) Record sections showing the emergent Rayleigh wave energy for all the possible long-term cross-correlation combinations associated with stations UE.UMZA, XX.STN25, UE.GHWR, and AE.SHM (see Figure S1 for locations) and all other possible station pairs. Note that the positive and negative correlation lags have been averaged and phase-velocity dispersion measurements performed on the symmetric component. (b) Example of picking of the fundamental mode for a phase dispersion curve identified from the filtered cross-correlation between station IR.LAR1 (Iran) and UE.MZWR (southwest UAE). Picked phase velocities, with relative uncertainties, are represented by black dots. Top-right inset indicates station names (see Figure S1 for location).

Coupled with a number of seismic stations in Iran, continuous seismic data recorded from a new network in the UAE represent a unique opportunity to examine and relate patterns of crustal and mantle anisotropy to dynamics in a region of convergence of orogenic belts. Here, we constrain anisotropy in the crust using ambient seismic noise recordings, and account for the apparent azimuthal dependence of measured Rayleigh-wave phase velocities to test whether orogenic processes have left an imprint in the Strait of Hormuz syntaxis. To constrain the strength (delay time) and orientation (fast axis) of anisotropy in the underlaying mantle, we calculate the differential arrival time between orthogonal components of core seismic phases from teleseismic earthquakes. We then reconcile both the recovered isotropic velocities and anisotropic orientations to different deformational events that have controlled the structural styles in the lithosphere beneath the seismic network. In particular, surface geological evidence suggests that obduction of the Semail ophiolite occurred from NE to SW onto the proto-Arabian continental margin. Yet, geophysical methods have thus far not been able to image underthrusting of the continental lithosphere beneath the ophiolite sequence. However, if such underthrusting is present, it would be expected to manifest as a possible perturbation of the mantle flow, or as a "frozen-in" deformation in the tectonic fabric. It is the signature of this tectonic process that we hope to reveal from the anisotropy pattern in the upper mantle beneath the UAE-Oman mountains.

2. Data Analysis

2.1. Anisotropic Phase-Velocity Maps

Broadband continuous seismic records employed here are sourced from 68 seismic stations operating in the study region (Figures 1 and S1). Recording periods used in this study are generally 2.5 years, from June 2014 to December 2016 (Pilia et al., 2020b). Empirical Green's Functions (EGFs) and phase velocities are taken from Pilia et al. (2020b); a short summary of the processing carried out to obtain phase velocities from the raw, continuous ambient-noise records is presented in Text S1 and Figures S2 and S3. Figure 2 shows the symmetric component of the cross-correlations associated with a number of stations, along with an example of dispersion analysis to extract phase velocities.

To characterize the effects of azimuthal variations of the interstation-averaged phase velocities, we invert them and map the isotropic and anisotropic wavefield components over a period range of 5–25 s. The

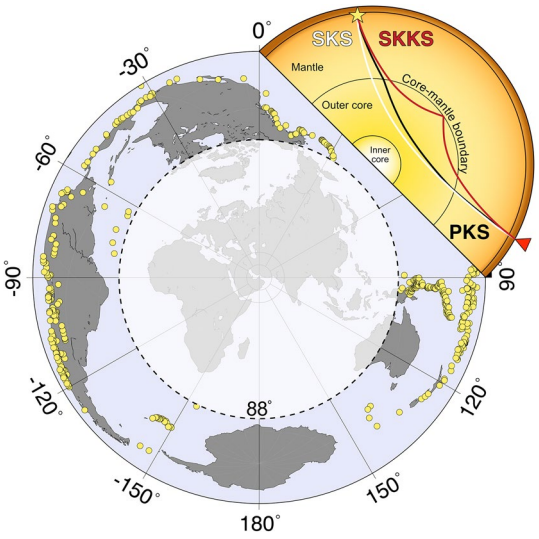

Figure 3. Teleseismic earthquakes used to measure XKS splitting (yellow dots). Seismic phases used in this study are illustrated in the top-right inset.

azimuthal dependence of local Rayleigh phase speed C in the presence of a weak anisotropic medium can be expressed via the following relation (Smith & Dahlen, 1973):

$$C(T) = C_0(T) + A_1(T)\cos(2\theta) + A_2(T)\sin(2\theta) + A_3(T)\cos(4\theta) + A_4(T)\sin(4\theta)$$

where $C_0\ (T)$ is the isotropic term at period T, θ is the ray propagation azimuth and A_1, A_2, A_3, and A_4 are azimuthal anisotropic coefficients. The terms 2θ and 4θ exhibit a periodicity of π and $\pi/2$, respectively, and account for the azimuthal variations. However, Montagner and Nataf (1986) have demonstrated that 4θ coefficients normally provide very little contribution to the azimuthal variability of Rayleigh wave phase velocities, hence are often ignored (Bao et al., 2016; Fry et al., 2010; Pilia et al., 2016; Rawlinson et al., 2014). Therefore, what we need to compute at any grid point of our model is a set of three unknowns, specifically $C_0\ (T)$, $A_1\ (T)$, and $A_2\ (T)$. We use the inversion scheme of Debayle and Sambridge (2004), which is based on the continuous parameterization algorithm of Montagner (1986). Smoothing regularization is imposed through application of an a priori spatial correlation filter among points separated by a L_{corr} distance, while an a priori model standard deviation σ controls the amplitude of anomalies, thus acting as a damping constraint on the final solution.

2.2. XKS-Phase Splitting

By entering into an anisotropic medium, a seismic shear wave splits into two quasi-shear wave components with orthogonal polarization that then travel with different speeds through the anisotropic medium. The heading component is polarized parallel to the fast symmetry axis of anisotropy. By arriving at a seismic station, the delay (split) time between the two components is an integral effect of the strength of anisotropy and the length traveled through the anisotropic medium. In a shear-wave splitting (SWS) analysis, the polarization of the fast component and the split time are measured and taken as a proxy for the symmetry axis and strength (proportional to the delay time) of the underlying anisotropic medium, respectively.

We use records of core-refracted shear phases (SKS, PKS, and SKKS, called hereinafter XKS) from a total of 462 teleseismic events in the epicentral distance range 88°–142° with magnitude larger than 5.7 (Figure 3). In an SWS analysis, the XKS waveforms at each station can be either individually or jointly processed. We exploit the SplitRacer code of Reiss and Rümpker (2017) to jointly analyze the XKS waveforms available from each station. The parameters of a one-layer anisotropy model beneath each station are searched to minimize the total energy of all T-components of XKS seismograms at the station. In addition, individual splitting parameters are estimated for each XKS waveform to verify the azimuthal variation of the parameters. The parameters of one-layer anisotropy for each station are presented here when the T-component energy reduction is more than 30% and these parameters are in agreement with the mean values of the individual splitting parameters. These parameters represent the anisotropic structure of a dominant layer that affects the XKS waves for the observed azimuths.

3. Results

3.1. Synthetic Resolution Tests of Tomographic Maps

Solution robustness assessment is useful to evaluate the spatial resolution and sensitivity of seismic features observed in tomographic models. Here, this is carried out through a series of synthetic resolution experiments designed to test the trade-off between isotropic and anisotropic variations in Rayleigh phase velocity. Resolution tests were initially performed separately for the isotropic and anisotropic components of the wavefield using a source-receiver configuration, as well as inversion parameters, identical to those for the observational data set. The study area is parameterized through a grid node spacing of 0.1° in latitude

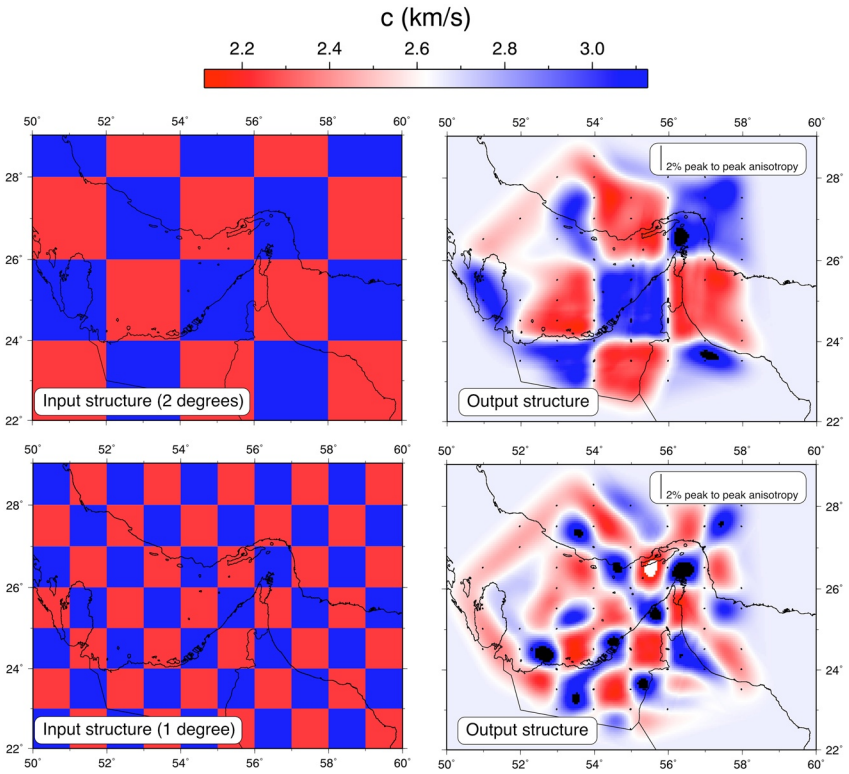

Figure 4. Comparison between input synthetic (1° and 2°) and output models for isotropic velocities at 10 s. In the input checkerboard model, the anisotropy is set to zero. The output structures show little evidence of spurious anisotropy.

and longitude. The starting velocity model is assumed to be isotropic and constant in the whole model space. This is implemented by associating the average phase velocity calculated for that particular period to each grid node, while the anisotropic coefficients are set to zero. The a priori data standard deviations and correlation lengths are set after analysis of the trade-off curves for each period (see Figure S4 for an example at 10 s). The a priori data standard deviation for the isotropic term was instead set to the phase-velocity uncertainty value determined for each individual measurement, which appears to correspond with the value obtained from the trade-off analysis (Figure S4). The noise is assumed to be uncorrelated, so the off-diagonal elements of the a priori data covariance matrix are zero and its diagonal elements are not all equal. An additional normally distributed error of 0.1 km/s was applied to each ray-path to simulate uncertainty associated with the observational data set and adjust the amplitude of the model perturbations. Synthetic data are then inverted using the same tomographic inversion procedure described earlier with the goal of faithfully reconstructing two predetermined synthetic checkerboard inputs: one purely isotropic that is parameterized through an alternating pattern of higher and lower wave-speed variations (Figure 4), and the other only containing anisotropic variations with alternating blocks of NS and EW orientations, or different sets of fast-velocity orientations—one at N45 and another at N135 (Figure 5). Independently inverting both sets of synthetic traveltimes makes it possible to investigate whether anisotropy or isotropy is respectively introduced in the recovered models, when we previously assumed they are not required by the data. Additionally, we jointly invert for isotropic and anisotropic terms (as done with the observational data set), including synthetic structures that resemble those observed in our tomographic models. We include a 0.6 km/s variation from low to high velocity across the Semail thrust, and include a complex blocky variation of anisotropy orientations at 10 s (Figure 6).

Figure 4 shows that the checkerboard velocity pattern is fairly well recovered through the isotropic inversion, particularly with structures as large as 2°, although it does contain potentially misleading artifacts in peripheral regions. This is an expected effect due to the combination of lower ray-path coverage, deficiency of crossing paths information, and a locally dominant orientation of seismic raypaths, which have a

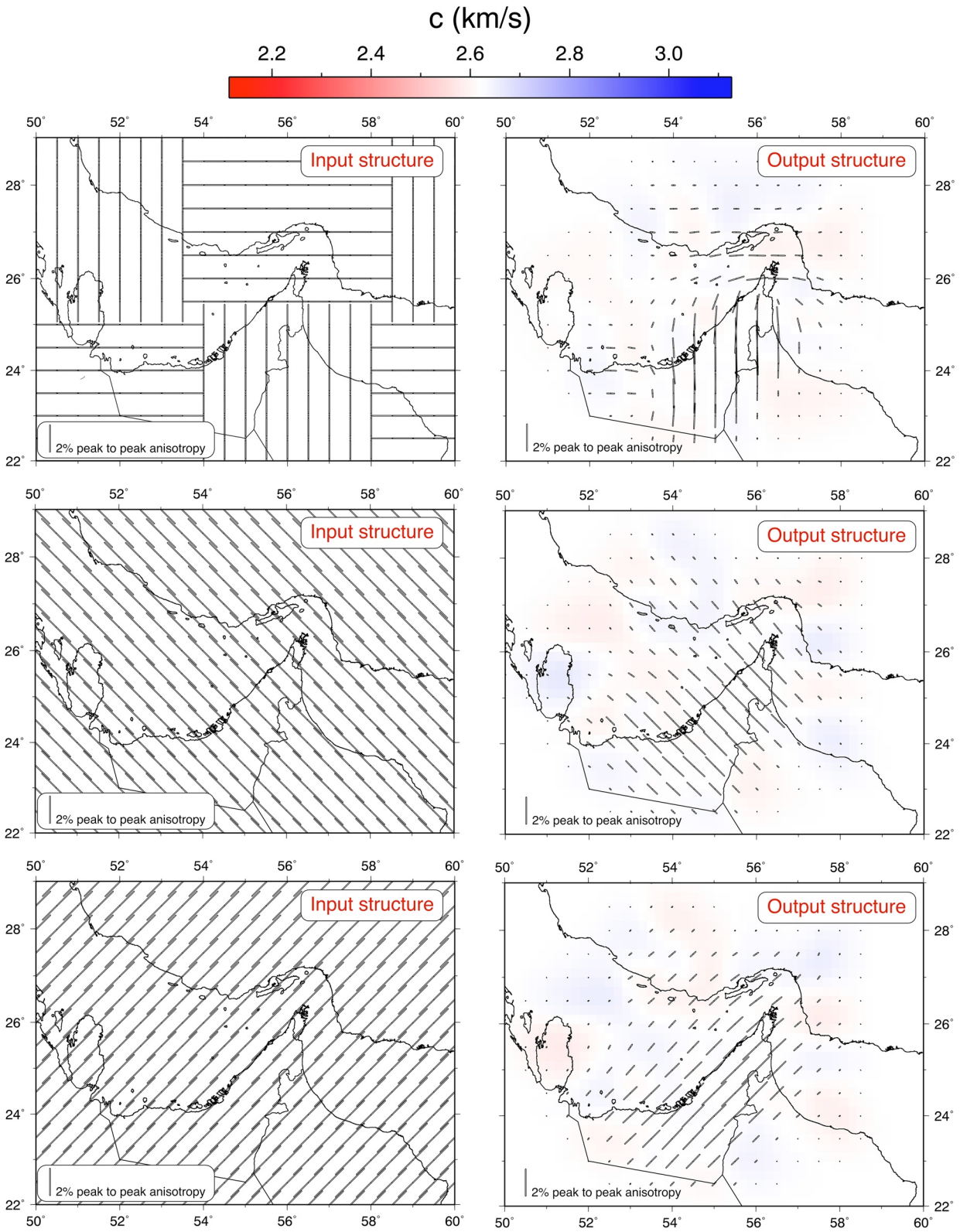

Figure 5. Comparison between input synthetic and output models for anisotropic terms at 10 s for the study area. In the input checkerboard model, the isotropy term is set to zero. The output structures show little evidence of spurious isotropy.

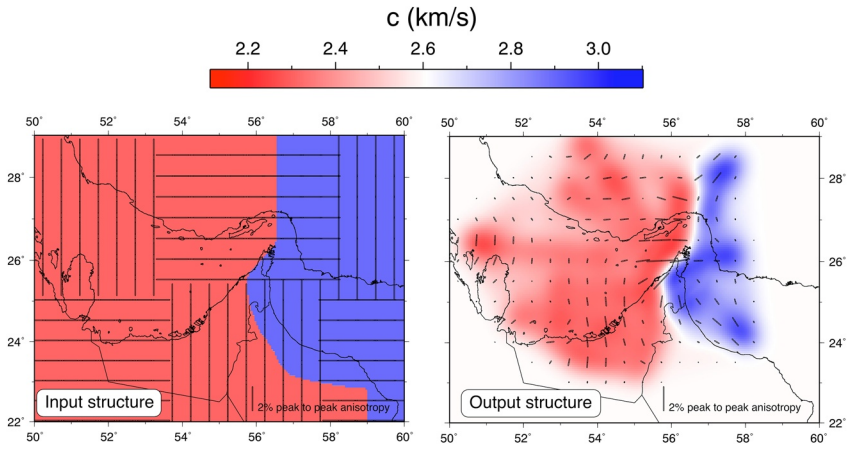

Figure 6. Synthetic test results from input synthetic structure involving a complex pattern of anisotropic terms and a strong, sharp velocity discontinuity. Isotropic and anisotropic terms are jointly inverted here (as per the observational data set).

tendency to smear out velocity anomalies in a specific direction. This is evident, for example, in the westernmost study area, where input structures are reproduced as elongated streaks and blurry anomalies. It can be noticed that the amount of spurious anisotropy introduced during the inversion is minimal throughout the model. Similarly, the recovery of the anisotropic NS and EW fast directions is good (Figure 5), with the exception of western and eastern edge regions.

The retrieved models only see the appearance of relatively minor isotropic variations. A common feature in the isotropic and anisotropic input checkerboard patterns is that the interface between individual blocks exhibits a sharp discontinuity. Such dramatic changes are generally difficult to retrieve and result in a smooth transition through near-zero anisotropy at the edge of each block (anisotropic model) or smooth velocity variation (isotropic model). This is, however, not surprising as it is an intrinsic property of regularized iterative non-linear schemes, hence a direct consequence of the inversion method used. Another common feature is that the pattern of anomalies is normally more reliable than their absolute amplitude. When anisotropy and isotropy are jointly inverted (Figure 6), resulting output structure shows that the strong isotropic velocity discontinuity is well recovered, although it is not surprising that sharp anisotropic variations (i.e., 90°) are slightly smoothed where strong discontinuities occur.

Overall, if a strong velocity change is present across the Semail thrust, this can be faithfully recovered by our data set and inversion method. Similarly, a 90° contrast of anisotropy orientations in the northernmost Musandam peninsula can be recovered.

3.2. Tomographic Model

Figure 7 shows the crustal structure beneath the northeastern Arabian plate margin via a series of Rayleigh phase-velocity tomographic maps, onto which the orientation of the fast axes of anisotropy have been superimposed. We present period-dependent maps at 5, 10, 15, and 25 s, which are broadly representative of the uppermost and lower crust (see sensitivity kernels in Figure 7). The study area is parameterized using the same grid node spacing, a priori model standard deviation, and L_{corr} specified for the resolution tests (see Section 3.1). The starting velocity model is assumed to be isotropic and constant in the whole model space by assigning to each grid node the average phase velocity determined for that particular period. The data variance is on average reduced by 70% in the isotropic solution model.

The regional pattern of isotropic phase-velocity variations reveals the presence of a high-velocity area that spatially correlates with the surface expression of the UAE-Oman mountain belt. This feature runs approximately landward of the eastern UAE and Oman shoreline and appears to be flanked by low-velocity anomalies. Indeed, phase velocities decrease by about 1 km/s where the flanking Persian Gulf and the Gulf of Oman are known to be dominated by thick sedimentary basins.

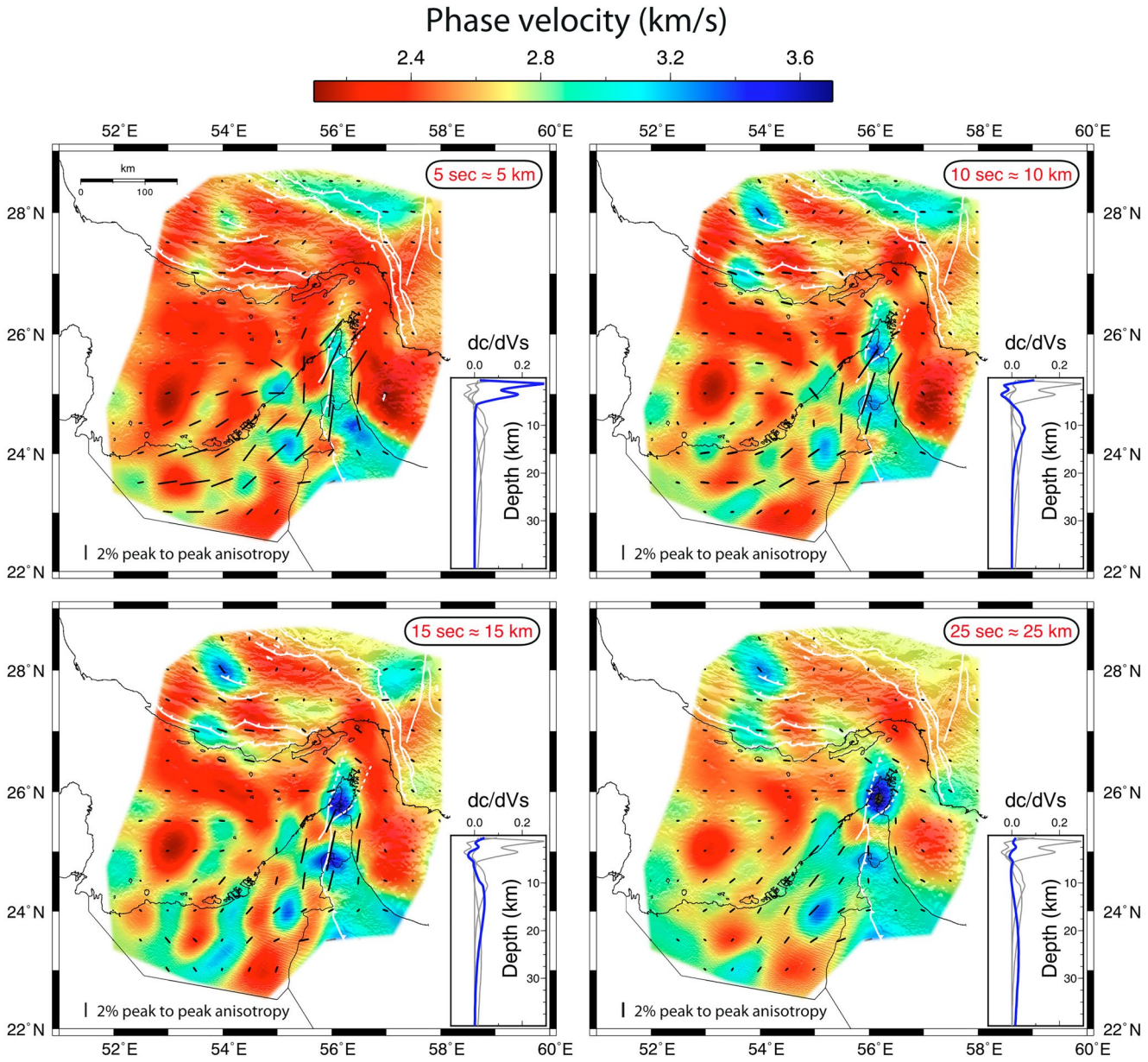

Figure 7. Final 2-D phase-velocity maps as a function of period illustrating both the isotropic (absolute variations of velocity) and anisotropic (black bars) components of the wave velocity field. Peak sensitivity of Rayleigh phase velocity occurs at a depth (in km) approximately equal to the period (in seconds), as shown by the sensitivity kernels (blue lines—gray lines are for comparison with other periods) in the bottom right inset of each map.

A prominent feature of the fast-azimuthal anisotropy directions, particularly at shallow to mid-crustal depths, is the sharp change occurring from the Musandam peninsula to the Zagros mountains (Figure 7). The fast directions are mostly trending nearly north-south in the UAE-Oman mountain belt to approximately WNW in the Strait of Hormuz and ZFTB. This divergence, however, should be viewed with caution since the more heterogeneous station coverage in Iran might be resulting in less robust anisotropy strength and directions in the Zagros, as shown in Figures 5 and 6. Further to the southwest, fast anisotropy axes return to a dominantly northeast-southwest and east-west trend.

3.3. Robustness of XKS Measurements

As described in Section 2.2, we perform a joint analysis of XKS waveforms recorded at each station. When searching for the parameters of a one-layer model, the main assumption is that the XKS waves are mainly affected by anisotropy structure of a single layer within the range of the observed azimuths. To verify this assumption, we examined the azimuthal variation of the individual splitting parameters. A systematic azimuthal variation of splitting parameters for each station is taken as the first-order indication of depth-dependent anisotropy (Rümpker & Silver, 1998; Silver & Savage, 1994). However, as typical with temporary seismic networks, our limited azimuthal coverage does not allow for a full azimuthal coverage at most of the stations. Despite the limited azimuthal coverage, examination of the individual measurements indicates that the mean values of these measurements are in the agreement with parameters for the one-layer model obtained from the joint analysis. This examination suggests that the XKS are mainly affected by one layer of anisotropy within the observed azimuths.

The joint-analysis approach described in Section 2.2 allows to invert for two layers of anisotropy (azimuthal coverage permitting), albeit inverting for the splitting parameters for two-layer models is known to be a highly non-unique process (e.g., Latifi et al., 2018). As we are equipped with crustal anisotropy results from surface-wave tomography, we examine the effect of crustal anisotropy on the XKS splitting observation at a number of stations with adequate azimuthal coverage. At these locations, we search for two-layer models by fixing the fast direction of the upper layer in the direction of crustal anisotropy, as constrained by surface waves (Figure S5). The theoretical curves of the two-layer models (Figure S5) show that crustal anisotropy could cause the occurrence of apparently extreme values of XKS splitting parameters but at azimuths where we have only limited observations. Our two-layer modeling suggests that the effect of crustal anisotropy on our XKS analysis and one-layer inversion is negligible. Furthermore, the projection of individual splitting parameters onto two representative depths of 75 and 170 km (Figure S6 and S7) exhibits insignificant azimuthal variation of single measurements. This indicates that a one-layer model is a good approximation for the XKS observations at the majority of our stations.

3.4. XKS Splitting Parameters

Final results from our XKS analysis are shown in Figure 8, along with the splitting parameters in Table 1. Delay times across the region are on average 1.0 s, rather heterogeneously distributed and do not seem to follow an organized pattern. On the other hand, the dominant splitting orientation beneath the UAE-Oman mountains is remarkably consistent with an average orientation of 15° anticlockwise from the north, suggesting that in this location a single, broad anisotropic feature is being resolved. Elsewhere, an approximately NE-SW orientation appears to dominate the pattern of anisotropy in the upper mantle.

4. Discussion

4.1. Seismic Wavespeed and Anisotropy in the Crust

A consequence of the thrust-sheet load from the Semail ophiolite was the development of a peripheral bulge and flexure of the pre-existing underlying rift margin, with establishment of a foreland basin (Ali et al., 2020; Ali & Watts, 2009; Robertson, 1987; Warburton et al., 1990). Following the end of the obduction loading process, a so-called "hinterland" (ten Brink & Stern, 1992) basin (up to 10 km thick—Ali et al., 2020; Pilia et al., 2021; Ravaut et al., 1998) also developed from subsidence in the Gulf of Oman. Tomographic maps in Figure 7 reveal a high-velocity body that spatially correlates to the UAE-Oman mountain belt, and is bounded to the east and west by two low wave-speed anomalies, which we attribute to these flanking sedimentary basins. Similarly, sediments of the proto-Arabian passive margin in the Persian Gulf and the ZFTB dominate the tomographic images with slower wavespeeds. The eastern extent of the northern Semail ophiolite, marked in our tomographic maps as a strong lateral variation from high to low phase velocity, runs offshore in the vicinity of the coastline and concur with the location proposed by Ali et al. (2020), Pilia et al. (2020a), and Pilia et al. (2021). At all periods, we observe a transition from relatively slow to fast wavespeeds near the surface expression of the MZTF, highlighting a difference in seismic character between the Arabian Platform and central Iran. As discussed in Pilia et al. (2020b), this

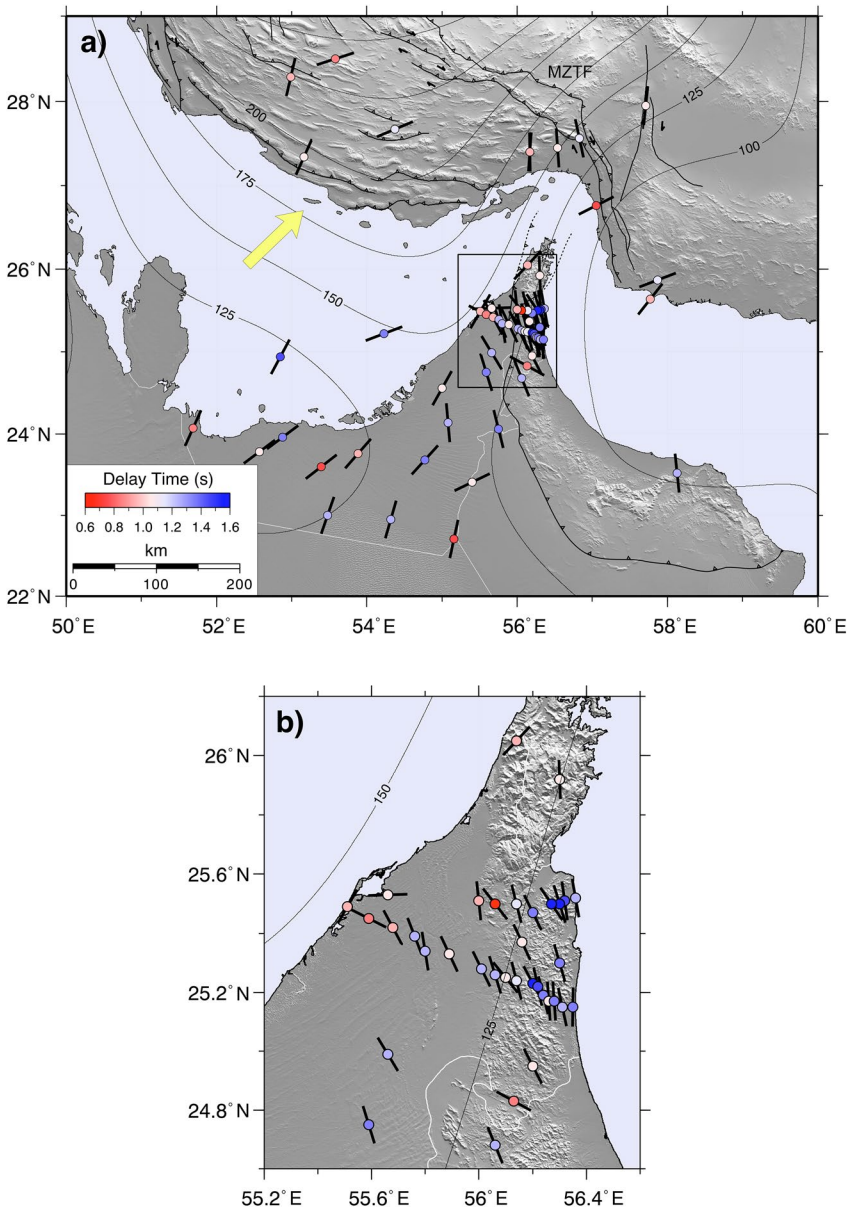

Figure 8. Results from XKS analysis. (a) XKS measurements at our stations with absolute plate motion of 45.26 mm/year (yellow arrow—ITRF reference frame from Altamimi et al. [2016]), and lithospheric thickness contour lines from Priestley and McKenzie (2013). (b) Zoom-in on the two transects across the Musandam Peninsula.

is the only area of the southern Zagros where low-angle thrusting earthquakes occur beyond the MZTF and extend to a depth of 30 km.

A somewhat surprising feature of the isotropic velocity variations is the high-velocity region revealed at 25 s beneath the northernmost Musandam peninsula. As shown in Figure 1, this area is limited by the Hagab thrust to the west, and the Dibba fault to the east, and does not currently contain exposure of the Semail ophiolite. However, the ophiolite thrust sheet almost certainly overthrust the Musandam shelf carbonates, although it was eroded off during the post-Oligoene uplift and Musandam culmination (Searle et al., 2014). This may indicate that the crust could be relatively thinner here. Detailed information about crustal thickness beneath northern Musandam Peninsula is lacking, although some poorly constrained estimates place it at around 30 km (Kaviani et al., 2020). Therefore, it is reasonable to believe that 25 s period waveforms

Table 1
Splitting Parameters for Stations Shown in Figure 8

Station	Sta_Lat	Sta_Lon	Phi	*dt*
AE.AJN	24.56	55.00	29	1.0
AE.ALN	24.06	55.75	−14	1.3
AE.JRN	24.94	52.85	28	1.4
AE.MSF	25.37	56.16	−25	1.0
AE.MZR	23.00	53.48	19	1.2
AE.SHM	26.05	56.14	43	0.9
AE.SRB	25.22	54.23	69	1.3
AE.UMQ	25.53	55.66	88	1.0
BI.BNDS	27.40	56.17	−1	0.9
BI.CHBR	25.60	60.48	4	0.8
BI.GHIR	28.29	52.99	13	0.9
DN.FAQ	24.75	55.59	−17	1.3
DN.HAT	24.83	56.13	−61	0.8
DN.NAZ	24.99	55.66	−31	1.2
II.UOSS	24.95	56.20	−27	1.0
IR.BNB	27.45	56.54	−4	1.0
IR.GENO	27.40	56.17	4	0.9
IR.JASK	25.87	57.87	69	1.1
IR.JHRM	28.50	53.58	72	0.8
IR.JSK1	25.64	57.77	38	0.9
IR.KHNJ	27.95	57.71	6	1.0
IR.KHSK	26.76	57.05	63	0.7
IR.LAR1	27.67	54.37	67	1.1
IR.LMD1	27.34	53.16	24	1.0
IR.NGCH	25.36	61.14	26	1.1
IR.NIAN	27.56	56.83	−12	1.1
IR.SRVN	27.40	62.40	−43	1.1
OM.ASH	24.68	56.06	−22	1.2
OM.BAN	25.92	56.30	−2	1.0
OM.BID	23.52	58.13	−6	1.2
OM.MDH	25.30	56.30	−16	1.3
OM.SOH	24.13	56.53	19	1.1
UE.GHWR	23.96	52.88	53	1.3
UE.MZWR	23.76	53.88	41	0.9
UE.SLWR	24.07	51.69	24	0.8
UE.UMZA	22.71	55.16	12	0.7
XX.STN01	25.49	55.51	30	0.9
XX.STN02	25.45	55.59	−63	0.8
XX.STN03	25.42	55.68	−28	0.9
XX.STN04	25.39	55.76	−21	1.2
XX.STN05	25.34	55.80	−9	1.2
XX.STN06	25.33	55.89	−25	1.0
XX.STN07	25.28	56.01	−26	1.2

sample the uppermost part of the mantle, although it is also possible that high velocities exist in the lower crust.

In the northern UAE-Oman orogenic belt, the fast azimuths of anisotropy appear to delineate a curved trend following the Dibba Fault and the Semail Thrust front, indicating parallelism between tectonic structure and anisotropy orientations. This implies that the seismic anisotropy we observe in the northern UAE-Oman belt, a region where Figures 5 and 6 demonstrate the model is well resolved, may be related to the tectonic fabric. However, we recognize that the direction of anisotropy is also similar to the strike of sheeted dikes (Nicolas et al., 2000) and the crystallographic preferred orientation of olivine found in the obducted Tethys upper mantle (Ambrose et al., 2018). Though, it is important to keep in mind that the Semail ophiolite is relatively thin in onshore (Ali et al., 2020; Pilia et al., 2021). Both stress-aligned shape-preferred orientation (SPO) and lattice preferred orientation (LPO) of the ophiolite aggregate minerals may therefore be contributing to the observed anisotropy. As the maximum horizontal stress directions (in excess of 45°) inferred from the World Stress Map (Heidbach et al., 2016) show no parallelism with our anisotropy directions in the upper crust of the orogenic belt, we can potentially exclude the contribution of cracks in originating the observed anisotropy.

A striking feature of our tomographic results is the change in the fast-propagation traces from approximately WNW in the ZFTB and northern tip of the Musandam peninsula, to nearly NS in the UAE-Oman belt, which appears to be a fairly consistent pattern throughout the crust (Figures 7, 9 and 10). In this region, the fast anisotropy axes support parallelism between tectonic fabric and anisotropy orientations. Orogen-parallel anisotropy observed in our tomographic model concurs with previous interpretations using seismic anisotropy at orogenic belts. For example, Fry et al. (2010) identified azimuthal anisotropy orientations to be normal to the direction of thrusting in the central Alps. Similarly, Pilia et al. (2016) and Bao et al. (2016) observed orogen-parallel anisotropy in the Tasmanides of Australia and the Cordillera (western Canada), respectively.

Since the western area of the UAE is obscured by a thick layer of Quaternary sand dunes, it is impossible to infer any structural trend from the surface geological record. Comparison of the maximum horizontal stress directions, inferred from local borehole breakouts and drilling-induced tensile fractures (Noufal et al., 2016), with the anisotropy orientations at 5 and 10 s periods (Figure 7) yields an average difference of 20° in the onshore area and 70° in the offshore. We then exclude the hypothesis that cracks contribute to the observed anisotropy. Compression from the Zagros collisional system is unlikely to have left an imprint in the tectonic fabric of the southwestern UAE crust. The pattern of anisotropy revealed here can potentially be explained by the structure inherited from extensional stresses (Kendall et al., 2006) that initiated faulting and rifting of the Arabian plate margin during the Mesozoic (i.e., ENE anisotropy directions orthogonal to spreading direction). Indeed, previous normal faults in this region appear to have been reactivated as thrust faults during the continental collision in the Zagros (Jackson, 1980). Therefore, it is not surprising that the strike of the structures detected in the Persian Gulf and southwest UAE resemble that of thrust faults found in the southern Zagros.

Table 1
Continued

Station	Sta_Lat	Sta_Lon	Phi	*dt*
XX.STN08	25.26	56.06	−17	1.2
XX.STN09	25.25	56.10	−39	1.0
XX.STN10	25.24	56.14	−14	1.1
XX.STN11	25.23	56.20	−28	1.5
XX.STN12	25.22	56.22	−12	1.4
XX.STN13	25.19	56.24	−14	1.3
XX.STN14	25.17	56.26	−4	1.0
XX.STN15	25.17	56.28	−4	1.3
XX.STN16	25.15	56.31	−12	1.2
XX.STN17	25.15	56.35	1	1.3
XX.STN18	25.52	56.36	−10	1.2
XX.STN19	25.51	56.32	−8	1.4
XX.STN20	25.50	56.30	−17	1.5
XX.STN21	25.50	56.27	−34	1.5
XX.STN22	25.47	56.20	−26	1.3
XX.STN23	25.50	56.14	−14	1.1
XX.STN24	25.50	56.06	−38	0.6
XX.STN25	25.51	56.00	−6	0.9
XX.STN27	24.14	55.08	−5	1.2
XX.STN28	23.68	54.77	42	1.3
XX.STN29	23.41	55.40	64	1.0
XX.STN30	22.95	54.32	16	1.2
XX.STN31	23.60	53.39	52	0.7
XX.STN32	23.78	52.57	53	1.0

4.2. Mantle Deformation Beneath the Semail Ophiolite

By assuming that the lower mantle is not the main contributor to SKS splitting observations, we seek to explain our observations of mantle anisotropy in terms of lithospheric deformation and asthenospheric flow (Figures 8–10). Plate-driven viscous drag in the asthenosphere, for example, is typically advocated when fast-splitting orientations align with absolute plate motion (e.g., Savage, 1999). In the southwestern study area, which is underlain by the stable Precambrian Arabian basement, and beneath the ZFTB, the fast polarization orientations are consistent with the direction of Arabian plate motion (Figure 8). In contrast, seismic azimuthal anisotropy beneath the UAE-Oman mountain range is evidently diverging from the plate motion direction (approximately 60°). Considering the relatively short length-scales variations in fast XKS polarization orientations (e.g., from 24.56°N–55.0°E to 25.64°N–57.77°E), which imply shallow sources of anisotropy (Alsina & Snieder, 1995), we seek to explain this pattern by invoking fossil anisotropy in the lithospheric mantle.

Previous surface wave tomographic studies identified a large contrast in lithospheric thickness, ranging from 90 km in the Gulf of Oman, to 250 km beneath the southcentral ZFTB (Priestley et al., 2012). This transition could potentially rework patterns of mantle flow through the generation of edge-driven convection (e.g., Ramsay & Pysklywec, 2011). In our results, such flow would be expected as either null-splitting where downwelling is predicted at the lithospheric discontinuity (or where there is a lack of lithospheric fabric), or at least as discontinuity-parallel splitting due to lateral flow. The latter is observed in the well-developed eastern Himalayan syntaxis, where both GPS velocities and mantle flow orientations wrap around the Namche Barwa syntaxis (Flesh et al., 2005), following indentation of the Indian plate. Since our observations suggest a dominant SE-NW-oriented seismic anisotropy in this region with little evidence for two layers of mantle anisotropy, we argue that the Strait of Hormuz syntaxis may disturb the asthenospheric flow but is not capable of modifying it.

While a number of stations in the eastern side of the seismic transects across the UAE-Oman mountain belt exhibit relatively high delay times, others do not. Additionally, when inspecting Figure 8, one can note that immediately to the north and south of the profiles there are a number of stations at similar longitude (e.g., II.UOSS, DN.HAT, and OM.BAN) with fairly low delay times (about 1 s or lower delay times). These would not be expected if delay times followed a hypothetical increasing trend from the foreland area to the mountains. Also, it is unlikely that a lithospheric thickness variation of 25 km (which is about the vertical resolution of the tomographic model of Priestley et al. [2012]) can result in a delay-time variation of around 1 s. In Figure S8, the splitting parameters are plotted against longitude, and confirm that the above-mentioned trend, if present, is very subtle, similar to the results obtained by Kaviani et al. (2021) for the Zagros Mountains.

Geological and geochronological data suggest that the Semail ophiolite formed above a NE-dipping subduction zone 96–95 Ma (Rioux et al., 2016) and was emplaced from NE to SW onto the previously rifted Mesozoic continental margin of Arabia from 95 to at least 79 Ma (Searle et al., 2003). In the UAE, the lower crust appears to be composed of tightly folded and thrust granulite-facies rocks formed at pressure-temperature conditions of 11–15 kbar and 770°C–900 °C at 94.5–90 Ma (Searle et al., 2015). In the eastern part of the Oman mountains, meta-basic sills intruded into Permian limestones along the NE margin were transformed to eclogites at the deepest structural level (As Sifah eclogites) indicating subduction of the leading edge of the continental margin to depths of ~80–90 km at least in the eastern Oman mountains segment (Searle, 2007; Warren et al., 2003). Following exhumation of the high-temperature granulites in the UAE and high-pressure eclogites at As Sifah in Oman, the whole obduction process ended by ~68 Ma with Upper

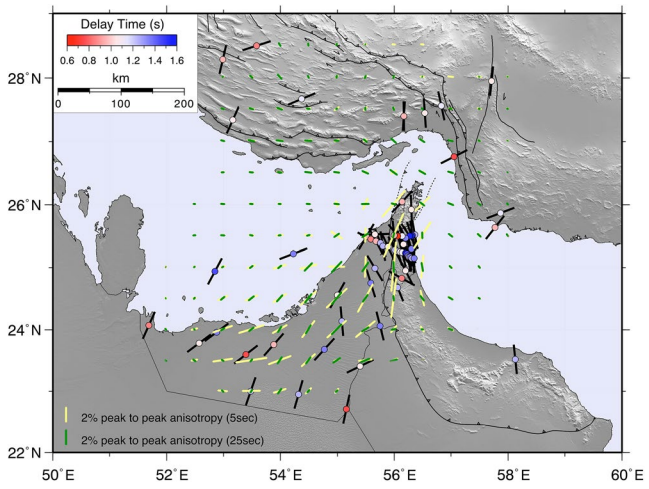

Figure 9. Comparison of azimuthal anisotropy orientations from seismic tomography (5 and 25 s periods as per Figure 7) and XKS measurements (as per Figure 8).

Maastrichtian clastic sediments unconformably overlying all units. This is the last significant deformational episode recorded throughout the Oman Mountains, except for a Miocene-Pliocene uplift event that formed a large-scale fold structure and enhanced the Cretaceous culmination of Jebel Akhdar and Saih Hatat. A return to stable, shallow marine conditions from Upper Maastrichtian to Eocene time was followed by post-Eocene gentle folding of the entire mountains. In the north, culmination of the Musandam shelf carbonates above the Hagab thrust occurred during the Oligocene-Early Miocene. Offshore seismic lines clearly show the tip lines of this thrust and the Musandam fold structures truncated by the mid-Miocene unconformity beneath the Upper-Miocene Fars Formation (Searle et al., 2014). We argue that the persistent fast-polarization orientations localized in the UAE-Oman mountains region derive from the frozen-in deformation inherited from the continental lithospheric mantle during the NE-directed underthrusting of the Arabian passive margin (Figure 10).

5. Conclusions

A new seismic network in the UAE has allowed us to constrain crustal and mantle deformation using anisotropic tomography and SWS analysis. The compelling degree of consistency between the orientation of fast anisotropy axes and tectonic fabric seen in the crust, marking a rotation of ~90° from the southern Zagros to the UAE-Oman belt, is a record of diachronous deformation associated with transition from Late Cretaceous ophiolite obduction to Eocene early continental collision. It is likely that the two orthogonal anisotropy orientations revealed by our model stem from the orogenic processes relative to obduction of the Semail ophiolite and continental collision in the Zagros mountains. Consistency between fast-polarization orientations localized in the UAE-Oman belt and the strike of the Oman subduction zone suggests that the anisotropy signature in the lithospheric mantle has retained a pattern that dates back to the time of Late Cretaceous obduction of the Semail ophiolite (Figure 10). Our data corroborate previous geological evidence on the geometry of the NE-dip of the Oman

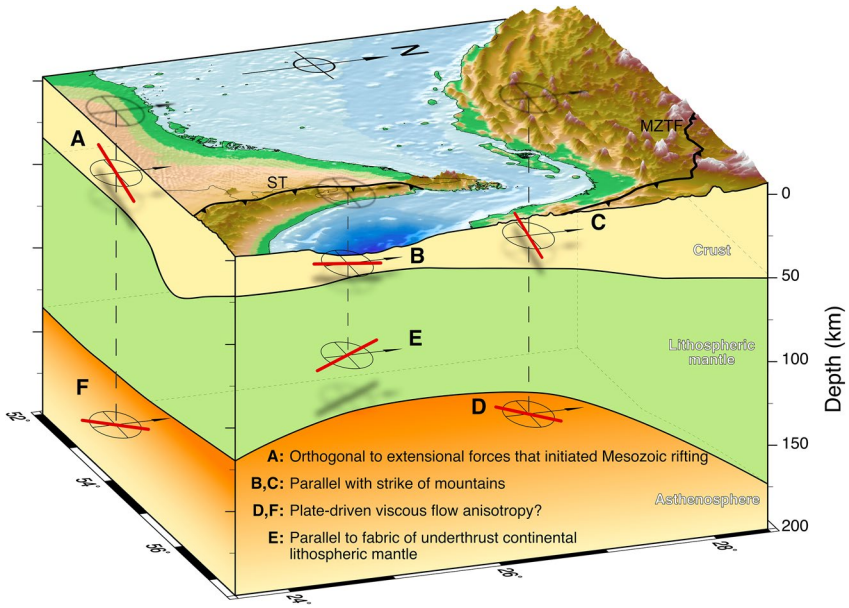

Figure 10. Conceptual illustration summarizing the anisotropy orientations observed in the lithosphere beneath the study area. Red bars are dominant orientations of anisotropy. Crustal thickness is consistent with Ali et al. (2020), Kaviani et al. (2020), and Pilia et al. (2021). Lithospheric thickness is consistent with Priestley and McKenzie (2013). ST, Semail thrust.

subduction system, the orthogonal emplacement of thrust sheets, and provides the first direct geophysical evidence from the mantle lithosphere.

Data Availability Statement

Data acquisition in the UAE was partially supported by The Petroleum Institute Research Centre Project LTR14011. The authors thank Brook Keats and Tyler Ambrose for insightful discussions about the tectonics of the Semail ophiolite. We are grateful to the Iranian Seismological Center and NCM for providing daily noise records from broadband stations in Iran and the remaining stations used in this study, respectively. The data set used in this study is from Pilia et al. (2020b).

Acknowledgments
S. Pilia acknowledges support from the Natural Environmental Research Council (NERC) Grant NE/R013500/1 and from the European Union's Horizon 2020 Research and Innovation Program under Marie Skłodowska-Curie Grant Agreement 790203.

References

Agard, P., Omrani, J., Jolivet, L., Whitechurch, H., Vrielynck, B., Spakman, W., et al. (2011). Zagros orogeny: A subduction-dominated process. *Geological Magazine*, *148*(5–6), 692–725. https://doi.org/10.1017/S001675681100046X

Ali, M. Y., Aidarbayev, S., Searle, M. P., & Watts, A. B. (2017). Subsidence history and seismic stratigraphy of the western Musandam peninsula, Oman-United Arab Emirates mountains. *Tectonics*, *37*(1), 154–181. https://doi.org/10.1002/2017TC004777

Ali, M. Y., & Watts, A. B. (2009). Subsidence history, gravity anomalies and flexure of the United Arab Emirates (UAE) foreland basin. *GeoArabia*, *14*(2), 17–44.

Ali, M. Y., Watts, A. B., Searle, M. P., Keats, B., Pilia, S., & Ambrose, T. (2020). Geophysical imaging of ophiolite structure in the United Arab Emirates. *Nature Communications*, *11*(1), 1–10. https://doi.org/10.1038/s41467-020-16521-0

Alsina, D., & Snieder, R. (1995). Small-scale sublithospheric continental mantle deformation: Constraints from SKS splitting observations. *Geophysical Journal International*, *123*(2), 431–448. https://doi.org/10.1111/j.1365-246X.1995.tb06864.x

Altamimi, Z., Rebischung, P., Métivier, L., & Collilieux, X. (2016). ITRF2014: A new release of the International Terrestrial Reference Frame modeling nonlinear station motions. *Journal of Geophysical Research: Solid Earth*, *121*, 6109–6131. https://doi.org/10.1002/2016JB013098

Ambrose, T. K., Wallis, D., Hansen, L. N., Waters, D. J., & Searle, M. P. (2018). Controls on the rheological properties of peridotite at a palaeosubduction interface: A transect across the base of the Oman-UAE ophiolite. *Earth and Planetary Science Letters*, *491*, 193–206. https://doi.org/10.1016/447j.epsl.2018.03.027

Babuska, V., & Cara, M. (1991). *Seismic anisotropy in the Earth* (Vol. 10). Springer.

Bao, X., Eaton, D. W., & Gu, Y. J. (2016). Rayleigh wave azimuthally anisotropic phase velocity maps beneath western Canada. *Journal of Geophysical Research: Solid Earth*, *121*(3), 1821–1834. https://doi.org/10.1002/2015JB012453

Carminati, E., Aldega, L., Smeraglia, L., Scharf, A., Mattern, A., Albert, R., & Gerdes, A. (2020). Tectonic evolution of the Northern Oman Mountains, part of the Straits of Hormuz Syntaxis: New structural and paleothermal analyses and U-Pb dating of synkinematic calcite. *Tectonics*, *39*(4), e2019TC005936. https://doi.org/10.1029/2019TC005936

Crampin, S. (1994). The fracture criticality of crustal rocks. *Geophysical Journal International*, *118*(2), 428–438. https://doi.org/10.1111/j.1365-246X.1994.tb03974.x

Debayle, E., & Sambridge, M. (2004). Inversion of massive surface wave data sets: Model construction and resolution assessment. *Journal of Geophysical Research: Solid Earth*, *109*(B2), B02316. https://doi.org/10.1029/2003JB002652

Flesch, L. M., Holt, W. E., Silver, P. G., Stephenson, M., Wang, C. Y., & Chan, W. W. (2005). Constraining the extent of crust–mantle coupling in central Asia using GPS, geologic, and shear wave splitting data. *Earth and Planetary Science Letters*, *238*(1–2), 248–268. https://doi.org/10.1016/j.epsl.2005.06.023

Fry, B., Deschamps, F., Kissling, E., Stehly, L., Giardini, D., & Heidbach, O. (2010). Layered azimuthal anisotropy of Rayleigh wave phase velocities in the European Alpine lithosphere inferred from ambient noise. *Earth and Planetary Science Letters*, *297*(1–2), 95–102. https://doi.org/10.1016/j.epsl.2010.06.008

Glennie, K., Boeuf, M., Clarke, M. H., Moody-Stuart, M., Pilaar, W., & Reinhardt, B. (1973), Late Cretaceous nappes in Oman Mountains and their geologic evolution. *AAPG Bulletin*, *57*(1), 5–27.

Heidbach, O., Rajabi, M., Reiter, K., Ziegler, M., & Wsm Team. (2016). World stress map database release 2016. GFZ Data Services.

Jackson, J. (1980). Reactivation of basement faults and crustal shortening in orogenic belts. *Nature*, *283*(5745), 343–346. https://doi.org/10.1038/283343a0

Kaviani, A., Mahmoodabadi, M., Rümpker, G., Pilia, S., Tatar, M., Nilfouroushan, F., et al. (2021). Mantle-flow diversion beneath the Iranian plateau induced by Zagros' lithospheric keel. *Scientific Reports*, *11*(1), 1–12. https://doi.org/10.1038/s41598-021-81541-9

Kaviani, A., Paul, A., Moradi, A., Mai, P. M., Pilia, S., Boschi, L., et al. (2020). Crustal and uppermost mantle shear-wave velocity structure beneath the Middle East from surface-wave tomography. *Geophysical Journal International*, *221*, 1349–1365. https://doi.org/10.1093/gji/ggaa075

Kendall, J. M., Pilidou, S., Keir, D., Bastow, I. D., Stuart, G. W., & Ayele, A. (2006). Mantle upwellings, melt migration and the rifting of Africa: Insights from seismic anisotropy. *Geological Society, London, Special Publications*, *259*(1), 55–72. https://doi.org/10.1144/GSL.SP.2006.259.01.06

Latifi, K., Kaviani, A., Rümpker, G., Mahmoodabadi, M., Ghassemi, M. R., & Sadidkhouy, A. (2018). The effect of crustal anisotropy on SKS splitting analysis—Synthetic models and real-data observations. *Geophysical Journal International*, *213*(2), 1426–1447. https://doi.org/10.1093/gji/ggy053

Montagner, J. (1986). Regional three-dimensional structures using long-period surface waves. *Annals of Geophys*, *4*(B3), 283–294.

Montagner, J.-P., & Nataf, H.-C. (1986). A simple method for inverting the azimuthal anisotropy of surface waves. *Journal of Geophysical Research: Solid Earth*, *91*(B1), 511–520. https://doi.org/10.1029/JB091iB01p00511

Morris, A., Meyer, M., Anderson, M. W., & MacLeod, C. J. (2016). Clockwise rotation of the entire Oman ophiolite occurred in a suprasubduction zone setting. *Geology*, *44*(12), 1055–1058. https://doi.org/10.1130/G38380.1

Nicolas, A., Boudier, F., Ildefonse, B., & Ball, E. (2000). Accretion of Oman and United Arab Emirates ophiolite—Discussion of a new structural map. *Marine Geophysical Researches*, *21*(3), 147–180. https://doi.org/10.1023/A:1026769727917

Noufal, A., Obaid, K., & Ali, M. (2016). Abu Dhabi stress map. ADIPEC. SPE-182919.

Pilia, S., Ali, M. Y., Searle, M. P., Watts, A. B., Lü, C., & Thompson, D. A. (2021). Crustal structure of the UAE-Oman mountain range and Arabian rifted passive margin: New constraints from active and passive seismic methods. *Journal of Geophysical Research: Solid Earth*, *126*(4), e2020JB021374. https://doi.org/10.1029/2020JB021374

Pilia, S., Arroucau, P., Rawlinson, N., Reading, A. M., & Cayley, R. A. (2016). Inherited crustal deformation along the East Gondwana margin revealed by seismic anisotropy tomography. *Geophysical Research Letters*, *43*(23), 12082–12090. https://doi.org/10.1002/2016GL071201

Pilia, S., Hu, H., Ali, M. Y., Rawlinson, N., & Ruan, A. (2020a). Upper mantle structure of the northeastern Arabian Platform from teleseismic body-wave tomography. *Physics of the Earth and Planetary Interiors*, *307*, 106549. https://doi.org/10.1016/j.pepi.2020.106549

Pilia, S., Jackson, J. A., Hawkins, R., Kaviani, A., & Ali, M. Y. (2020b). The southern Zagros collisional orogen: New insights from transdimensional-trees inversion of seismic noise. *Geophysical Research Letters*, *47*(4), e2019GL086258. https://doi.org/10.1029/2019GL086258

Priestley, K., & McKenzie, D. (2013). The relationship between shear wave velocity, temperature, attenuation and viscosity in the shallow part of the mantle. *Earth and Planetary Science Letters*, *381*, 78–91. https://doi.org/10.1016/j.epsl.2013.08.022

Priestley, K., McKenzie, D., Barron, J., Tatar, M., & Debayle, E. (2012). The Zagros core: Deformation of the continental lithospheric mantle. *Geochemistry, Geophysics, Geosystems*, *13*(11), Q11014. https://doi.org/10.1029/2012GC004435

Ramsay, T., & Pysklywec, R. (2011). Anomalous bathymetry, 3D edge driven convection, and dynamic topography at the western Atlantic passive margin. *Journal of Geodynamics*, *52*(1), 45–56. https://doi.org/10.1016/j.jog.2010.11.008

Ravaut, P., Carbon, D., Ritz, J. F., Bayer, R., & Philip, H. (1998). The Sohar Basin, Western Gulf of Oman: Description and mechanisms of formation from seismic and gravity data. *Marine and Petroleum Geology*, *15*(4), 359–377. https://doi.org/10.1016/s0264-8172(98)00055-5

Rawlinson, N., Arroucau, P., Musgrave, R., Cayley, R., Young, M., & Salmon, M. (2014). Complex continental growth along the proto-Pacific margin of East Gondwana. *Geology*, *42*(9), 783–786. https://doi.org/10.1130/G35766.1

Reiss, M. C., & Rümpker, G. (2017). SplitRacer: MATLAB Code and GUI for semiautomated analysis and interpretation of teleseismic shear-wave splitting. *Seismological Research Letters*, *88*(2A), 392–409. https://doi.org/10.1785/0220160191

Rioux, M., Garber, J., Bauer, A., Bowring, S., Searle, M., Kelemen, P., & Hacker, B. (2016). Synchronous formation of the metamorphic sole and igneous crust of the Semail ophiolite: New constraints on the tectonic evolution during ophiolite formation from high-precision U-Pb zircon. *Earth and Planetary Science Letters*, *451*, 185–195. https://doi.org/10.1016/j.epsl.2016.06.051

Robertson, A. H. F. (1987). Upper Cretaceous Muti Formation: Transition of a Mesozoic nate platform to a foreland basin in the Oman Mountains. *Sedimentology*, *34*(6), 1123–1142. https://doi.org/10.1111/j.1365-3091.1987.tb00596.x

Rümpker, G., & Silver, P. G. (1998). Apparent shear-wave splitting parameters in the presence of vertically varying anisotropy. *Geophysical Journal International*, *135*(3), 790–800. https://doi.org/10.1046/j.1365-246X.1998.00660.x

Savage, M. K. (1999). Seismic anisotropy and mantle deformation: What have we learned from shear wave splitting? *Reviews of Geophysics*, *37*(1), 65–106. https://doi.org/10.1029/98RG02075

Searle, M. (2019). *Geology of the Oman mountains, Eastern Arabia* (p. 478). Springer.

Searle, M. P. (1988). Structure of the Musandam culmination (Sultanate of Oman and United Arab Emirates) and the Straits of Hormuz syntaxis. *Journal of the Geological Society*, *145*(5), 831–845. https://doi.org/10.1144/gsjgs.145.5.0831

Searle, M. P. (2007). Structural geometry, style and timing of deformation in the Hawasina Window, Al Jabal al Akhdar and Saih Hatat culminations, Oman Mountains. *GeoArabia*, *12*(2), 99–130.

Searle, M. P. (2015). Mountain building, tectonic evolution, rheology, and crustal flow in the Himalaya, Karakoram, and Tibet. In G. Schubert (Ed.), *Treatise of geophysics* (Vol. 6, pp. 469–511). https://doi.org/10.1016/B978-0-444-53802-4.00121-4

Searle, M. P., Cherry, A. G., Ali, M. Y., & Cooper, D. J. (2014). Tectonics of the Musandam Peninsula and northern Oman Mountains: From ophiolite obduction to continental collision. *GeoArabia*, *19*(2), 135–174.

Searle, M. P., Warren, C. J., Waters, D. J., & Parrish, R. R. (2003). Subduction zone polarity in the Oman Mountains: Implications for ophiolite emplacement. *Geological Society, London, Special Publications*, *218*(1), 467–480. https://doi.org/10.1144/GSL.SP.2003.218.01.24

Searle, M. P., Waters, D. J., Garber, J. M., Rioux, M., Cherry, A. G., & Ambrose, T. K. (2015). Structure and metamorphism beneath the obducting Oman ophiolite: Evidence from the Bani Hamid granulites, Northern Oman mountains. *Geosphere*, *11*(6), 1812–1836. https://doi.org/10.1130/GES01199.1

Silver, P. G., & Savage, M. K. (1994). The interpretation of shear-wave splitting parameters in the presence of two anisotropic layers. *Geophysical Journal International*, *119*(3), 949–963. https://doi.org/10.1111/j.1365-246X.1994.tb04027.x

Smith, M. L., & Dahlen, F. (1973). The azimuthal dependence of Love and Rayleigh wave propagation in a slightly anisotropic medium. *Journal of Geophysical Research*, *78*(17), 3321–3333. https://doi.org/10.1029/JB078i017p03321

Stern, R. J., & Johnson, P. (2010). Continental lithosphere of the Arabian Plate: A geologic, petrologic, and geophysical synthesis. *Earth-Science Reviews*, *101*(1–2), 29–67. https://doi.org/10.1016/j.earscirev.2010.01.002

ten Brink, U., & Stern, T. (1992). Rift flank uplifts and hinterland basins: comparison of the Transantarctic Mountains with the Great Escarpment of southern Africa. *Journal of Geophysical Research: Solid Earth*, *97*(B1), 569–585. https://doi.org/10.1029/91JB02231

Tilton, G. R., Hopson, C. A., & Wright, J. E. (1981). Uranium-lead isotopic ages of the Samail ophiolite, Oman, with applications to Tethyan ocean ridge tectonics. *Journal of Geophysical Research: Solid Earth*, *86*(B4), 2763–2775. https://doi.org/10.1029/JB086iB04p02763

Warburton, J., Burnhill, T. J., Graham, R. H., & Isaac, K. P. (1990). The evolution of the Oman Mountains foreland basin. In A. H. F. Robertson, M. P. Searle, & A. C. Ries (Eds.), *The geology and tectonics of the Oman region. Geological Society of London, Special Publication* (Vol. 49, pp. 419–427). https://doi.org/10.1144/gsl.sp.1992.049.01.26

Warren, C. J., Parrish, R. R., Searle, M. P., & Waters, D. J. (2003). Dating the subduction of the Arabian continental margin beneath the Semail ophiolite, Oman. *Geology*, *31*(10), 889–892. https://doi.org/10.1130/G19666.1

References From the Supporting Information

Schimmel, M., Stutzmann, E., & Gallart, J. (2011). Using instantaneous phase coherence for signal extraction from ambient noise data at a local to a global scale. *Geophysical Journal International*, *184*(1), 494–506. https://doi.org/10.1111/j.1365-246X.2010.04861.x

Ventosa, S., Schimmel, M., & Stutzmann, E. (2017). Extracting surface waves, hum and normal modes: Time-scale phase-weighted stack and beyond. *Geophysical Journal International*, *211*(1), 30–44. https://doi.org/10.1093/gji/ggx284

Yao, H., van Der Hilst, R. D., & De Hoop, M. V. (2006). Surface-wave array tomography in SE Tibet from ambient seismic noise and two-station analysis—I. Phase velocity maps. *Geophysical Journal International*, *166*(2), 732–744. https://doi.org/10.1111/j.1365-246X.2006.03028.x